

# Star-forming blue ETGs in two newly discovered galaxy overdensities in the HUDF at $z=1.84$ and $1.9$ : unveiling the progenitors of passive ETGs in cluster cores

Simona Mei<sup>1,2,3</sup>, Claudia Scarlata<sup>4</sup>, Laura Pentericci<sup>5</sup>, Jeffrey A. Newman<sup>6</sup>, Benjamin J. Weiner<sup>6</sup>, Matthew L. N. Ashby<sup>6</sup>, Marco Castellano<sup>5</sup>, Christopher J. Conselice<sup>7</sup>, Steven L. Finkelstein<sup>9</sup>, Audrey Galametz<sup>5</sup>, Norman A. Grogan<sup>8</sup>, Anton M. Koekemoer<sup>8</sup>, Marc Huertas-Company<sup>1,2</sup>, Caterina Lani<sup>7</sup>, Ray A. Lucas<sup>8</sup>, Casey Papovich<sup>11</sup>, Marc Rafelski<sup>3</sup>, Harry I. Tepliz<sup>3</sup>

## ABSTRACT

We present the discovery of two galaxy overdensities in the HST UDF: a proto-cluster, HUDFJ0332.4-2746.6 at  $z = 1.84 \pm 0.01$ , and a group, HUDFJ0332.5-2747.3 at  $z = 1.90 \pm 0.01$ . The velocity dispersion of HUDFJ0332.4-2746.6 implies a mass of  $M_{200} = (2.2 \pm 1.8) \times 10^{14} M_{\odot}$ , consistent with the lack of extended X-ray emission. Neither overdensity shows evidence of a red sequence. About 50% of their members show interactions and/or disturbed morphologies, which are a signature of merger remnants. Most of their morphologically classified ETGs have blue colors and show recent star-formation. These observations reveal for the first time large fractions of spectroscopically confirmed star-forming blue ETGs in proto-clusters at  $z \approx 2$ . These star-forming ETGs are most likely among the progenitors of the quiescent population in clusters at more recent epochs. Their mass-size relation is consistent with that of passive ETGs in clusters at  $z \sim 0.7 - 1.5$ . If these galaxies are the progenitors of cluster ETGs at these lower redshifts, their size would evolve according to a similar mass-size relation. It is noteworthy that quiescent ETGs in clusters at  $z = 1.8 - 2$  also do not show any significant size evolution over this redshift range, contrary to field ETGs. The ETG fraction of our sample is  $\lesssim 40\%$ , compared to the typical quiescent ETG fraction of  $\approx 80\%$  in cluster cores at  $z < 1$ . The fraction, masses and colors of the newly discovered ETGs imply that other cluster ETGs will be formed/accreted at later time.

*Subject headings:* Galaxy Clusters : general

<sup>1</sup>GEPI, Observatoire de Paris, Section de Meudon, 5 Place J. Janssen, 92190 Meudon Cedex, France

<sup>2</sup>Université Paris Denis Diderot, 75205 Paris Cedex 13, France

<sup>3</sup>Infrared Processing and Analysis Center, California Institute of Technology, Pasadena, CA 91125, USA

<sup>4</sup>University of Minnesota

<sup>5</sup>INAF, Osservatorio Astronomica di Roma, Via Frascati 33, 00040 Monteporzio, Italy

<sup>6</sup>Harvard-Smithsonian Center for Astrophysics, 60 Garden Street, Cambridge, MA 02138, USA

<sup>7</sup>School of Physics and Astronomy, University of Nottingham, Nottingham, NG7 2RD, UK

<sup>8</sup>Space Telescope Science Institute, Baltimore, MD,

## 1. Introduction

Galaxy clusters are the largest structures observed in the Universe. Their distribution and (baryonic and dark) matter content constrain the cosmological model, and the study of their galaxy

USA

<sup>9</sup>The University of Texas at Austin, 2515 Speedway, Stop C1400, Austin, Texas 78712, USA

<sup>10</sup>University of Pittsburgh

<sup>11</sup>George P. and Cynthia Woods Mitchell Institute for Fundamental Physics and Astronomy, Texas A&M University, 4242 TAMU, College Station, TX 77743, USA

properties reveals the influence of dense environments on galaxy evolution.

Galaxies in clusters typically show a predominant early-type population and a red sequence (old stellar population) up to redshift  $z \approx 1.5 - 2$  (e.g., Kodama et al. 2007; Mei et al. 2009; Andreon & Huertas-Company 2011; Papovich et al. 2010; Snyder et al. 2012; Stanford et al. 2012; Zeinman et al. 2012; Gobat et al. 2013; Muzzin et al. 2013; Mantz et al. 2014). Most of the clusters observed in the local Universe have assembled their current early-type galaxy population at those redshifts (e.g., Cohn & White 2005; Li et al. 2007; Chiang et al. 2013). The redshift range around  $z \approx 1.5 - 2$ , however, has remained largely unexplored until recently. The reason is that surveys based on cluster X-ray emission or the Sunyaev Zel'dovich effect (SZ) lack depth and/or area to reach detections of typical clusters at these redshifts, and ground-based optical spectroscopy would require excessive exposure times to confirm them spectroscopically when detected in the infrared/far-infrared bandpasses.

In the past five years, cluster samples at  $z > 1.5$  have been significantly enlarged by the advent of deep and large enough surveys in the infrared and mid-infrared, such as GOODS-MUSIC (Castellano et al. 2007), the IRAC Distant Cluster Survey (IDCS; Eisenhardt et al. 2008; Stanford et al. 2012; Zeinman et al. 2012), the Spitzer Deep, Wide-Field Survey (SDWFS; Ashby et al. 2009), the Spitzer SPT Deep Field (SSDF; Ashby et al. 2013a), the Spitzer Adaptation of the Red-sequence Cluster Survey (SpARCS; Muzzin et al. 2013), Spitzer Wide-Area Infrared Extragalactic (SWIRE; Papovich et al. 2010), and the Clusters Around Radio-Loud AGN program (CARLA; Galametz et al. 2012; Wylezalek et al. 2013). Other cluster candidates have been identified around low luminosity radio sources (Chiaberge et al. 2010). Spectroscopic capability to confirm redshifts has been enhanced by optical and infrared grism spectroscopy with the Wide Field Camera 3 (WFC3) on the Hubble Space Telescope (HST), and infrared ground-based multi-object spectroscopy with the VLT/KMOS (Sharples et al. 2006), the Keck MOSFIRE (McLean et al. 2010; 2012) and the SUBARU MOIRCS (Ichikawa et al. 2006) instruments.

Until now, most clusters detected at  $z > 1.5$

have been identified as overdensities of red galaxies (e.g., Gladders & Yee 2000), then confirmed by spectroscopic follow-up of at least 5 members within 2 Mpc (e.g., Castellano et al. 2007, 2011; Kurk et al. 2009; Papovich et al. 2010; Tanaka et al. 2010; Stanford et al. 2012; Zeinman et al. 2012; Muzzin et al. 2013), and/or by their X-ray emission (Andreon et al. 2010, 2011; Gobat et al. 2011; Santos et al. 2011). Four clusters have been spectroscopically confirmed at  $z \sim 1.8 - 2$ : JKCS 041 (Andreon et al. 2010; Newman et al. 2013), IDCS J1426+3508 (Stanford et al. 2012), IDCS J1433.2+3306 (Zeinman et al. 2012), and CL J1449+085 (Gobat et al. 2010; 2013). For all the clusters with  $z > 1.8$ , spectroscopic redshifts have been obtained with grism spectroscopy from HST/WFC3, after ground-based optical spectroscopy failed to obtain enough signal. These systems show large fractions ( $\approx 50\%$ ) of star-forming galaxies, indicating that most of the quenching of star formation observed at lower redshift had not yet occurred (Tran et al. 2010; Fassbender et al. 2011; Hayashi et al. 2011; Tadaki et al. 2012; Zeinman et al. 2012; Brodwin et al. 2013). Recent observations at these redshifts also suggest that the specific star formation of galaxies in dense regions becomes higher than that in the field, although not all results are consistent with the supposed reversal of the star-formation density relation (Elbaz et al. 2007; Cooper et al. 2008; Grützbauch et al. 2011; Hatch et al. 2011; Popesso et al. 2012; Andreon 2013; Gobat et al. 2013; Koyama et al. 2013; Strazzullo et al. 2013; Santos et al. 2014; Scoville et al. 2013; Tanaka et al. 2013; Ziparo et al. 2013).

Concerning the build-up of their early-type population, various studies have focused on the evolution of galaxies in clusters/dense environments from  $z \approx 2$  to the present, and compared it to the field (Rettura et al. 2010; Cooper et al. 2012; Mei et al. 2012; Papovich et al. 2012; Raichoor et al. 2012; Bassett et al. 2013; Huertas-Company et al. 2013ab; Lani et al. 2013; Newman et al. 2013; Poggianti et al. 2013; Shankar et al. 2013; Strazzullo et al. 2013; Vulcani et al. 2013; Delaye et al. 2014; Shankar et al. 2014). These results indicate that the median/average passive ETG sizes in clusters are not significantly larger (consistent within  $2\sigma$ ), and the analysis of the pop-

ulation with larger sizes suggests different morphological type (E, S0) fractions and/or recently quenched faint galaxies.

In this paper, we present the discovery of two galaxy overdensities at redshift  $z = 1.84$  and  $z = 1.9$  in the HST Ultra-Deep Field (HUDF; Beckwith et al. 2006) with observations from the Cosmic Assembly Near-infrared Deep Extragalactic Legacy Survey (CANDELS; PI: S. Faber, H. Ferguson; Koekemoer et al. 2011; Grogin et al. 2011), and the 3D HST survey (PI: P. van Dokkum; van Dokkum et al. 2013). In Sec. 2, we present the observations. In Sec. 3 we describe our spectroscopic sample selection. In Sec. 4 we present the newly discovered overdensities and estimate one structure’s mass. In Sec. 5, we study the stellar population and structural properties of their galaxies. In Sec. 6 we conclude and in Sec. 7 we summarize our results.

We adopt a  $\Lambda$ CDM cosmology, with  $\Omega_m = 0.3$ ,  $\Omega_\Lambda = 0.7$ ,  $h = 0.72$ . All magnitudes are given in the AB system (Oke & Gunn 1983; Sirianni et al. 2005). Stellar masses are estimated with a Chabrier initial mass function (Chabrier 2003).

## 2. Observations

The Hubble Ultra-Deep Field (HUDF; Beckwith et al. 2006) is a  $200'' \times 200''$  area with the deepest HST observations in multiple wavelengths. HUDF has been observed by several programs since the first HST Advanced Camera for Surveys (ACS) data release in 2004, including deep WFC3 images as part of the HUDF09 program (PI: G. Illingworth; Bouwens et al. 2011), CANDELS, 3D-HST and HUDF12 (PI: R. Ellis; Ellis et al. 2013; Koekemoer et al. 2013). CANDELS is a 902-orbit Multi-Cycle Treasury survey with the HST, completed in Cycle 20. The main instrument used by the survey is WFC3, with 3, 4 and 6 orbit exposures in imaging with the WFC3/F105W ( $Y_{105}$ ), F125W ( $J_{125}$ ), and F160W ( $H_{160}$ ) filter, respectively, and grism spectroscopy in the infrared (WFC3/IR) channel. Parallel observations were undertaken with the ACS. A combination of all the HUDF observations with ACS and WFC3 has been recently released by the eXtreme Deep Field (XDF) program (Illingworth et al. 2013). We will use the combined XDF images for the galaxy structural properties analysis, in particu-

lar imaging with ACS/WFC (Wide Field Camera) F775W, F814W and F850LP ( $i_{775}$ ,  $I_{814}$ ,  $z_{850}$ , respectively), for a total exposure time of 377.8 ks, 50.8 ks and 421.6 ks, respectively, and WFC3/IR  $J_{125}$  and  $H_{160}$  for a total exposure time of 112.5 ks and 236.1 ks, respectively. The ACS WFC resolution (pixel size) is  $0.05''/\text{pixel}$ , and its field of view is  $202'' \times 202''$ . WFC3/IR has a  $136'' \times 123''$  field of view, with a spatial resolution of  $0.13''/\text{pixel}$ . The images have been drizzled and registered to obtain ACS and WFC3 mosaic images with the same resolution of  $0.06''$ . The image reduction is described in detail in Illingworth et al. (2013). We have verified that our results do not change when using the HUDF12 release (Koekemoer et al. 2013).

For the spectroscopy, the HUDF has been observed by two HST Treasury programs with spectroscopic observations: the CANDELS and the 3D-HST program. The 3D-HST program, completed in Cycle 19, obtained deep spectroscopy of the HUDF with the WFC3/IR G141 grism. The grism spectroscopy from these two programs was recently released as combined reduced spectra that include 8 orbits of 3D-HST and 9 orbits of CANDELS supernova follow-up observations, for a total of 17 orbits of observations (Brammer et al. 2012). The WFC3/IR G141 grism has an efficiency larger than 30% in the wavelength range  $1.1 < \lambda < 1.65\mu\text{m}$ , a spatial resolution of  $0.13''/\text{pixel}$  and a dispersion of  $46.5\text{\AA}/\text{pixel}$ . Typical uncertainties are  $5\text{\AA}$  for the zero point and  $0.04\text{\AA}$  for the dispersion (Kuntschner et al. 2010). The spectra were extracted by independent software developed by the 3D-HST collaboration, as described in Brammer et al. (2012), and redshifts have been estimated using both grism spectroscopy and broad-band photometry for a combined spectro-photometric estimate. For the entire spectroscopic catalog, spectral features used to estimate redshifts include rest-frame H $\alpha$ , [O II] $\lambda 3727$ , [O III] $\lambda 5007$  emission lines, and the Balmer 4000 $\text{\AA}$  break. The 3D-HST spectroscopy covers an area of  $\sim 140'' \times 140''$  in the HUDF.

Near ultra-violet images (NUV) of the HUDF were obtained in a Hubble Space Telescope treasury program (hereafter UVUDF; Teplitz et al. 2013) using the WFC3/UVIS detector. This project obtained deep images of the HUDF in the F225W, F275W, and F336W filters. Data were obtained in two observing modes (as described in

Teplitz et al. 2013), with  $\sim 15$  orbits of integration per filter in each mode. For the current analysis, we use the half of the data that were obtained with the post-flash (the UVIS capability to add internal background light), to mitigate the effects of degradation of the charge transfer efficiency of the detectors (Mackenty & Smith 2012). The data were reduced using a combination of standard and custom calibration scripts (see Rafelski et al. 2014, in prep.), including the use of newly released software to correct for charge transfer inefficiency. The individual reduced exposures were then registered and combined following the methods developed for CANDELS (Koekemoer et al. 2011). The  $5\sigma$  rms sensitivities in an aperture with  $0''.2$  radius are 27.9, 27.9, and 28.3 mag in  $F225W$ ,  $F275W$ , and  $F336W$ , respectively. Photometry in the UV was measured in isophotal areas determined from the B-band detection image obtained with SExtractor in dual image mode (Bertin & Arnouts 1996).

### 3. Spectroscopic sample selection

Using the CANDELS and 3D-HST spectroscopic redshifts, we identified an initial galaxy overdensity in the HUDF at redshift  $z \approx 1.85$ .

To assess the quality of the spectra, we used both visual inspection, the published spectrophotometric analysis from the 3D-HST collaboration (Brammer et al. 2012), and the CANDELS Guo et al. (2013) photometric redshift catalog. For 3D-HST spectroscopy, we applied the shift  $z_{spec} = 0.005 \times (1 + z_{3DHST})$ , as suggested in the documentation of the 3D-HST data release (van Dokkum et al. 2013, 3D-HST data release documentation). The accuracy of the Guo photometric redshifts is estimated to be  $\delta_{z_{pz}} = 0.030 \times (1 + z)$  for  $H_{160} < 24$  mag and  $\delta_{z_{pz}} = 0.039 \times (1 + z)$  for  $H_{160} > 24$  mag, with a global outlier fraction of  $\approx 4\%$ . This gives typical photometric redshift errors of  $\sigma_{pz} = 0.09 - 0.1$  at  $z=1.8-1.9$  up to  $H_{160} \approx 26$  mag.

We (BW and SM) flagged each spectrum as (1) certain, (2) good independently of photometric redshift estimates, (3) good using photometric redshift estimates, (4) probable, (5) not usable. For this work, we only use certain and good spectroscopic grism redshifts (flag 1 to 3). We have been particularly attentive to the possible contam-

ination from misidentification of  $H\alpha$  emission as OIII, from the foreground cluster at  $z=1.096$  (Salimbeni et al. 2009), e.g., we have not considered two galaxies because they show a single line emission and their photometric redshifts would indicate a most probable redshift at  $z \sim 1$ . The lines detected with significant signal-to-noise ratio are specified in Table 1, and are mainly [O III] $\lambda 5007$  or the OIII doublet, and [H $\beta$ ] $\lambda 4861$ .

We found 24 galaxies within a radius  $R = 2'$  (that corresponds to a comoving radius of 1 Mpc at  $z \approx 1.8 - 1.9$ ) of the main overdensity center (see below), good quality spectra, and redshift in the range  $1.8 < z < 1.95$ . In this range, the grism redshift median statistical uncertainty is  $\approx 0.001$  (Brammer et al. 2012; Colbert et al. 2013). To the statistical uncertainty, we add a systematic of  $0.003 \times (1 + z_{spec})$ . We estimate the systematics from the median scatter when comparing spectroscopic redshifts measured by the CANDELS collaboration (BW) with spectrophotometric redshifts published by the 3D-HST collaboration (Brammer et al. 2012), in the redshift range  $z = 0.5 - 2.5$ . This systematic is larger than, but consistent with, the uncertainties obtained from the simulations by Colbert et al. (2013) and exactly the same as found by Gobat et al. (2013).

We searched the GOODS CDF-S master catalog<sup>1</sup> for spectroscopy from ground-based follow-up of the area. When grism redshifts are probable or not usable, and ground-based multiple line redshift measurements are available with average S/N per pixel  $> 3$  (Kurk et al. 2013), we use VLT/FORS2 redshift measurements instead of the grism spectroscopy. Eight galaxies with redshift in the range  $1.8 < z < 1.95$  have good quality GMASS VLT/FORS2 spectroscopy and respect our S/N criteria, and four have better quality than the grism spectra. We added the missing 4 to the 24 galaxies above, to obtain 28 galaxies with good quality spectra in the range  $1.8 < z < 1.95$ . The 3D-HST spectra of the cluster members were published by the 3D-HST collaboration (Brammer et al. 2012). The GMASS spectra were published in Kurk et al. (2013).

The selected spectroscopic members extend to magnitudes as faint as  $H_{160} \approx 25.7$  mag; however,

<sup>1</sup><http://www.eso.org/sci/activities/garching/projects/goods/MasterSpectroscopy.h>

the grism spectroscopy sample shows a marked decrease in number at magnitudes fainter than  $H_{160} \approx 24.5$  mag. At this magnitude,  $\approx 95\%$  of the CANDELS galaxies in the HUDF area (Guo et al. 2013) have a grism redshift estimation, and  $\approx 50\%$  have good quality flags from our classification above.

The UVUDF NUV images permitted us to confirm that the selected galaxies are at  $z \sim 1.8 - 1.9$ , since we expect them to be UVIS/ $F225W$  dropouts (see Tepliz et al. 2013) and to be detected in the  $F336W$  filter. Each candidate has been inspected visually by two of us (CS and SM). Two of the candidates, UDF-1898 and UDF-1909 are  $F336W$  dropouts, and could either be galaxies at higher redshift or too faint to be detected. We will not consider these two objects in the rest of our analysis, leaving 26 selected galaxies with redshift  $1.8 < z_{spec} < 1.95$ . In the appendix, we show the WFC3  $F225W$ ,  $F275W$ ,  $F336W$ , and ACS  $F435W$ ,  $I_{814}$  and WFC3  $J_{125}$  images for each candidate.

We describe in Table 1 all the selected galaxies, and identify them by their 3D-HST UDF ID (Brammer et al. 2012) or GMASS ID (Kurk et al. 2013).

#### 4. Newly discovered overdensities in the UDF

##### 4.0.1. Structure definition

As shown in Fig. 1, the redshifts of the 26 selected galaxies appear to follow a double Gaussian distribution. This is confirmed by a classical Kolmogorov-Smirnov test, skewness and kurtosis test and the two more robust asymmetry index (A.I.) and tail index (T.I.) described in Bird & Beers (1993) (as in e.g., Castellano et al. 2011).

To select the structure members, given the small number of galaxies, we fit a double Gaussian plus a background to the observed distributions. We took into account Poissonian uncertainties in the histogram and adopted a redshift bin of 0.01. The Gaussian fits give  $\bar{z} = 1.84 \pm 0.01$  and  $\bar{z} = 1.905 \pm 0.005$ , for the first and second structure, respectively. We obtain  $\bar{z} = 1.84 \pm 0.01$  and  $\bar{z} = 1.90 \pm 0.01$ , respectively, from a biweight mean redshift and standard deviation.

Selecting galaxies within  $3 \times \sigma_{\bar{z}}$  of the two

means, we obtained 18 spectroscopic members for the first Gaussian and 7 spectroscopic members for the second. One galaxy is not selected as part of the structures because its redshift is too low.

To better estimate the significance of the two redshift overdensities, we used the complete sample of certain and good (as defined above) spectroscopic grism redshifts from CANDELS and 3D-HST in the range  $1.3 < z < 2$ , and calculated both projected densities using Nth-nearest neighbor distances and galaxy overdensities. In both calculations, we have considered only galaxies brighter than  $H_{160} = 24.5$  mag. Since we do not have a large area, we will measure statistics in redshift bins, and in the HUDF area covered by the grism spectroscopy, that corresponds to a co-moving size of  $\sim 1$  Mpc.

For the first overdensity estimate, we measure projected densities using Nth-nearest neighbor distances defined as  $\Sigma_N = \frac{N}{\pi D_N^2}$  (e.g., Dressler et al. 1980).  $N$  is the number of neighbors,  $D_n$  is defined as the distance in Mpc to the Nth nearest neighbor. We have calculated  $\Sigma_N$  within redshift bins of amplitude 0.06 (e.g., within a distance in redshift space  $3 \times \sigma_{\bar{z}}$  from the biweight analysis) from  $z = 1.3$  to  $z = 2$ . Our background density estimates were stable in the range  $N = 3 - 7$ , with  $\Sigma_N^{bck} = 0.5 \pm 1$ . The structure at  $z = 1.84$  is an overdensity at  $\approx 20\sigma$  above the background density (stable for  $N = 5 - 7$ ). The structure at  $z = 1.9$  has a density at  $4 - 6\sigma$  above the background density for  $N = 3$  and 4, respectively. Given the smaller number of galaxies, this measurement is less stable at different  $N$ . Our results do not change if we enlarge the redshift range, and do not consider in the analysis the known cluster at  $z = 1.096$  (see above).

For the second overdensity estimate, we use the definition of galaxy contrast  $\delta_c = \frac{N_{gal} - N_{bkg}}{N_{bkg}}$ .  $N_{gal}$  is the number of galaxies in a given redshift bin, and  $N_{bkg}$  is the average number of background galaxies in the entire redshift range  $1.3 < z < 2$ . We obtain  $N_{bkg} = 0.6 \pm 0.9$  galaxies per redshift bin of 0.06. Even if we do not count  $> 3\sigma$  peaks in the redshift distribution, this might be an upper limit to the average background, since we already know that there are significant overdensities in this field (Salimbeni et al. 2009). For the first structure, 18 galaxies are a  $\sim 20\sigma$  galaxy overden-

sity. For the second, 7 galaxies are a  $\sim 7\sigma$  overdensity. These results are consistent with those from projected densities using Nth-nearest neighbor distances.

This analysis confirms the detection of the structure at  $z = 1.84$  as a significant galaxy overdensity. We call this structure HUDFJ0332.4-2746.6, and adopt as center the position of its brightest galaxy ( $H_{160} = 22.008 \pm 0.002$  mag) in its denser region of comoving size  $R = 500$  kpc ( $1'$  at this redshift), at [RA,DEC]=[53.155647,-27.779298]. Only one member (GMSS 220) is farther than  $R = 1'$  from this center.

The second overdensity is detected at  $4 - 7\sigma$ , and we will call it HUDFJ0332.5-2747.3. We adopt as center the position of the brightest galaxy ( $H_{160} = 22.463 \pm 0.002$  mag) in its denser region, at [RA,DEC]=[53.149298,-27.788534]. It is filamentary and more extended than the first structure, and its detection threshold is closer to that of a galaxy group (e.g., Tanaka et al. 2013) than a proto-cluster (e.g., Papovich et al. 2010; Gobat et al. 2011).

The positions of the structures' members are shown in Fig. 2.

The comoving distance between the two structures is  $\sim 100$  Mpc. At  $z \sim 2$ , the standard cosmological model predicts that the comoving extension of progenitors of clusters with present masses  $M > 10^{14} M_{\odot}$  can reach  $\sim 25$  Mpc<sup>3</sup> for the most massive clusters (Chiang et al. 2013; Shattow et al. 2013), so the two structures are not predicted to necessarily merge to form a present-day cluster.

#### 4.1. Proto-cluster Mass Estimate

To estimate the mass of HUDFJ0332.4-2746.6, we make the assumption that it has already virialized. With this assumption, the proto-cluster mass can be estimated from its velocity dispersion.

The line-of-sight cluster velocity dispersion can be highly anisotropic, and small samples lead to large systematic uncertainties (White et al. 2010). For HUDFJ0332.5-2747.3, we expect uncertainties in the proto-cluster velocity dispersion from anisotropies of  $\approx 10\%$ . The uncertainty on the mass estimate for HUDFJ0332.5-2747.3 is too large because of the smaller number of galaxies, and we do not attempt to measure it.

We measure the HUDFJ0332.4-2746.6 intrinsic velocity dispersion from its 18 members, following Danese et al. (1980). We add in quadrature the statistical and systematic uncertainties in redshift. From the proto-cluster intrinsic velocity dispersion, we obtain an estimate of the mass using Eq. (1) from the  $\Lambda$ CDM simulations in Munari et al. (2013):

$$M_{200} = \left( \frac{\sigma_{1D}}{A_{1D}} \right)^{1/\alpha} \frac{10^{15} M_{\odot}}{h(z)} \quad (1)$$

with the parameters  $A_{1D} = 1090 \pm 50$ , and  $\alpha = 0.3333$  (see also Evrard et al. 2008).  $\sigma_{1D}$  is the cluster line-of-sight velocity dispersion  $\sigma_{disp}$ , and  $h(z) = H(z)/(100 \text{ km/s})$ , where  $H(z)$  is the Hubble constant. Assuming virialization, this equation gives the relation between the total mass of a cluster in a radius  $R_{200}$ <sup>2</sup> and its velocity dispersion, and is obtained by using a Navarro, Frenk and White (1996) dark matter mass profile with different concentration parameters and different constant velocity anisotropies. The uncertainty in the coefficient  $A_{1D}$  takes into account the uncertainties in these simulation assumptions. From the cluster velocity dispersion we also derive  $R_{200}$  (Carlberg et al. 1997).

Following the classic Danese et al. (1980) computation of the proto-cluster intrinsic velocity dispersion, and its uncertainty, we obtain  $\sigma_{disp} = 780^{+180}_{-100}$  km/s. This corresponds to a mass  $M_{200} = 2^{+2}_{-1} \times 10^{14} M_{\odot}$ , and  $R_{200} = 1.0^{+0.3}_{-0.1}$  Mpc.

To take into account possible systematics due to the sample selection, we estimate the uncertainty on the cluster velocity dispersion, its mass and its virial radius by bootstrapping 1,000 times on the 18 cluster members. Specifically, we recalculated the three quantities,  $\sigma_{disp}$ ,  $M_{200}$ , and  $R_{200}$ , substituting all the initial sample with a sample of the same size extracted randomly from the initial sample. We obtain an intrinsic velocity dispersion of  $\sigma_{disp} = (730 \pm 260)$  km/s,  $M_{200} = (2.2 \pm 1.8) \times 10^{14} M_{\odot}$ , and  $R_{200} = (0.9 \pm 0.3)$  Mpc. This suggests that using the classic computation from Danese et al. (1980) does not take into account all uncertainties in the sample selection, and we will use these last estimates as more robust. If

<sup>2</sup>  $R_{200}$  is the radius at which the cluster mean density is 200 times the critical density.

we underestimated systematics on redshift measurements, our mass estimate becomes an upper limit.

When using other values of  $A_{1D}$ , obtained using two different models of the baryonic physics in Munari et al. (2013), our results do not significantly change. A systematic of  $\approx 10\%$  in velocity dispersion from the line-of-sight anisotropies would lead to a systematic of  $\approx 10 - 15\%$  in mass, in this range of velocity dispersion and mass, and does not change our results.

If we assume that the structure just started to separate from the Hubble flow (Steidel et al. 1998), we would obtain masses for both structures of the same order of magnitude ( $\approx 10^{14} M_{\odot}$ ), but with larger systematics due to the difficulty in estimating the three-dimensional volume that they cover with the available low resolution spectroscopy.

## 4.2. X-ray observations

We also checked the 3 Msec XMM and 4 Msec Chandra X-ray observations for both point sources associated with the galaxies in the two overdensities and for possible extended emission from the ICM.

The HUDFJ0332.4-2746.6 member UDF-2095 coincides with source # 512 in the 4 Msec catalog (Xue et al. 2011). It has a soft band flux of  $1.8 \times 10^{-17} \text{ erg/sec/cm}^2$  and a hardness ratio of 0.27. The catalog classifies the emission as *galaxy* so it is most probably associated with star formation rather than with AGN activity. There are other X-ray sources within the cluster region, of which one (# 505 from Xue et al. 2011) is extended but associated to a lower redshift galaxy ( $z=0.99$ ). There is no indication of diffuse extended emission coinciding with either overdensity position.

From the lack of extended X-ray emission we can place an upper limit on the X-ray luminosity of  $1-6 \times 10^{43} \text{ erg/s}$ , depending on the temperature assumed (in the range 1–3 KeV). If we use the cluster mass-luminosity derived by Rykoff et al. (2008), this corresponds to an upper limit in total mass of  $M_{200} < (1 - 3) \times 10^{14} M_{\odot}$ , consistent with our mass estimate from the velocity dispersion, given the uncertainties and the assumption of virialization.

## 5. Overdensity galaxy population

### 5.0.1. Morphologies

All structures' galaxies but two (see Table 1) show recent star formation. In Fig. 3 and Fig. 4, we show their color images. Most of the morphologies are disturbed, and often show asymmetry and/or asymmetric tails. Using the WFC3  $J_{125}$  imaging, which corresponds to the B rest-frame at  $z=1.84-1.9$ , we visually classified galaxies into two categories: ETGs and late-type galaxies (LTGs). We included compact galaxies in the ETG class, and irregular galaxies in the LTG class. We have 6 ETGs at  $z=1.84$ , plus UDF-3058 that we consider a ETG with an asymmetric tail, and 3 ETGs at  $z=1.9$ . UDF-1355 looks like an ETG in the B-band rest-frame but shows asymmetric features in the UV, so we classify it as LTG. We consider as reliable only ETGs brighter than  $H_{160} = 23.5 \text{ mag}$  (van der Wel et al. 2012; Kartaltepe et al. 2014). LTGs always reveal structure and are therefore all reliably classified (see also, e.g., Kartaltepe et al. 2014; Mortlock et al. 2014).

Among the candidates at  $z = 1.84$ , UDF-3058 has an ambiguous morphology, with a bulge-like appearance and an asymmetric tail that appears in the B rest-frame. We classify it as an ETG. One galaxy that we classify as ETG, UDF 2900, shows a double core in the UV.

For the 17 galaxies with  $H_{160} < 24.5 \text{ mag}$ , our classification is consistent with the CANDELS morphological classification from Kartaltepe et al. (2014) for all galaxies but one. UDF 669 is classified as ETG by Kartaltepe et al. (2014), and LTG by this work. This is a typical level of consistency among different classifiers/classification methods when the morphological classification include only two broad classes, ETGs and LTGs (e.g., Postman et al. 2005; Huertas-Company et al. 2009, 2011).

Two spectroscopic pairs are close companions, but we do not have enough spectral resolution to identify them as mergers. From Kartaltepe et al. (2014), two objects are classified as mergers ( $12^{+13}_{-8} \%$ ), seven as interacting ( $41 \pm 14 \%$ ), six as asymmetric ( $35^{+15}_{-13} \%$ ), four have tidal features ( $23^{+14}_{-10} \%$ ). UDF 3297 has been marked as having a double nucleus. All of this accounts for nine objects ( $53^{+14}_{-15} \%$  of the sample), because some objects have multiple features. It is interesting

that half of these galaxies are interacting or disturbed, showing signatures which are characteristic of merger remnants (see also results from, e.g., Lotz et al. 2013; Mortlock et al. 2014).

The fraction of confirmed early-type galaxies is at most  $38 \pm 10\%$  of the entire sample, against the typical  $\approx 80\%$  and  $\approx 50 - 80\%$  observed in galaxy clusters at  $z < 1.5$  and  $1.5 < z < 2$ , respectively, for galaxy masses  $M > 10^{10-10.5} \times M_\odot$  and total cluster mass  $M > 10^{14} \times M_\odot$  (e.g., Postman et al. 2005; Desai et al. 2007; Mei et al. 2009, 2012; Tran et al. 2010; Fassbender et al. 2011; Hayashi et al. 2011; Papovich et al. 2012; Tadaki et al. 2012; Zeinman et al. 2012; Brodwin et al. 2013). These results have to be taken as upper limits to the fractions of ETGs. In fact, we emphasize that we only consider as secure ETGs those galaxies with  $H_{160} < 23.5$  mag, e.g., 2 over the 5 ETGs.

#### 5.0.2. Galaxy Masses and Colors

We have used the Guo et al. (2013) photometric catalog to estimate galaxy masses and colors. This catalog includes observations from CANDELS HST/WFC3  $Y_{105}$ ,  $J_{125}$  and  $H_{160}$  data, combined with existing public data from the HUDF09 programs. In addition to WFC3 bands, the catalog also includes data from UV (U-band from both CTIO/MOSAIC and VLT/VIMOS), optical (HST/ACS F435W, F606W, F775W, F814W, and F850LP), infrared (HST/WFC3 F098M, VLT/ISAAC Ks, VLT/HAWK-I Ks), and Spitzer/IRAC 3.6, 4.5, 5.8, 8.0  $\mu\text{m}$  observations (from the GOODS and SEDS surveys: Fazio et al. 2004; Ashby et al. 2013b). We refer to Guo et al. (2013) for a detailed description of these observations. The catalog is based on source detection in  $H_{160}$ , and all photometry was matched using the public software TFIT (Laidler et al. 2007). The photometry reaches a  $5\sigma$  depth (within an aperture of radius  $0.17''$ ) of 29.7 mag in the HUDF region, with a completeness of 50% at 28.1 mag in  $H_{160}$ .

We estimated galaxy masses from the Guo et al. broadband photometry, using the public software Le Phare (Arnouts et al. 2002; Ilbert et al. 2006), based on a  $\chi^2$  spectral energy distribution (SED) fitting method. For our Le Phare input parameters, we followed Ilbert et al. (2010) and used the Chabrier IMF, Bruzual & Charlot (2003) templates, solar metallicity, an exponentially decaying

star formation with  $\tau$  in the range 0.1 to 5 Gyr, and a Calzetti et al. (2000) extinction law with  $E(B-V)$  in the range 0 to 0.5.

In Fig. 5 we show the color-magnitude and color-mass relations. All galaxies have masses in the range  $8.9 \lesssim \log_{10}(\frac{M}{M_\odot}) \lesssim 10.8$ , and all their colors, but one (UDF-463), which also does not show emission lines, are bluer than quiescent galaxies at these redshifts. In fact, at  $z=1.84$  and according to a Bruzual & Charlot (2003) simple, single starburst model with solar metallicity, we would expect a red sequence at  $(I_{814} - J_{125}) \approx 2.3$  mag, for a formation redshift  $z_f = 2.5$ . This value corresponds to the mean luminosity-weighted formation redshift usually derived for galaxies in clusters at  $z \approx 1 - 1.5$  (e.g., Mei et al. 2006ab; Mei et al. 2009, 2012; Snyder et al. 2012; Brodwin et al. 2013; and references therein). We show as a continuous line the color-magnitude relation at  $z \sim 1$  from Mei et al. (2009) passively evolved to  $z=1.84$ . The dashed lines show 3 times their total observed scatter ( $3 \times \sigma_{obs} \sim 0.2$ ). Hereafter, we define as *red* galaxies those that are redder than the passively evolved red sequence minus  $3 \times \sigma_{obs}$ . It is clear that most of the ETGs in these structures still need to be quenched.

Unlike the known clusters at  $z \approx 1.8 - 2$  (Stanford et al. 2012; Zeinman et al. 2012; Newman et al. 2013; Gobat et al. 2011, 2013) that show overdensities of  $\sim 10 - 15$  red galaxies, the two overdensities do not show an already formed red sequence. Only one of the structure galaxies has a color red enough to be considered as a red sequence galaxy at these redshifts.

Potential red sequence galaxies could have been missed in our analysis because we only selected star-forming galaxies, or only those with good quality spectra from the 3D-HST, CANDELS and GMASS catalogs. However, there are only three other red galaxies within  $1'$  from the proto-cluster and group centers from the GMASS, Guo et al. (2013), Kartaltepe et al. (2014) catalogs. All three have grism spectra that are at lower or higher redshift, and do not belong to the two overdensities.

We robustly confirm that the two structures do not have an already formed red sequence, within  $1'$  of the proto-cluster and group centers. We cannot exclude that the two overdensities are part



of larger overdensities with well defined red sequences, but which we cannot detect within the observed area.

### 5.0.3. Galaxy Structural Properties

As demonstrated by van der Wel et al. (2012), the WFPC3/IR camera resolution together with the depth of CANDELS observations, permit us to estimate galaxy structural parameters up to  $H_{160} \approx 23$  mag, and galaxy sizes up to  $H_{160} \approx 24.5$  mag. Basset et al. (2013) have also shown that the same applies up to  $J_{125} = 24$  mag.

We estimated galaxy structural parameters for all galaxies (ETGs and LTGs) using GALFIT (Peng et al. 2002; 2010) on the WFC3/IR  $J_{125}$  image from XUDF, that corresponds to the B-band rest-frame at  $z \sim 1.8 - 1.9$ . We have adopted a single Sersic profile, and did not constrain the values of the Sersic index  $n$  for most of the sample, as suggested in Peng et al. (2002). The point spread function (psf) model was provided by van der Wel et al. (2012). Most of the galaxies in our sample have Sersic index  $n < 2$  ( $\sim 90\%$  of the sample). As the size estimate, we use the circularized effective radius  $R_e$ , defined as the average half-light radius along the major axis of the best fitting galaxy model multiplied by the ratio between the minor and major axis  $q = \sqrt{b/a}$ .

Fig. 6 shows the galaxy mass-size relation. The two stars show the ETG mass-size relation observed in galaxy clusters at redshift  $1.2 < z < 1.5$  from Delaye et al. (2014), and the dark blue circles show results from Lani et al. (2013) ( $1 < z < 2$ ), for their most dense regions (see also Papovich et al. 2012; Basset et al. 2013). These previous works pointed out that ETGs in clusters have, on average, larger sizes than ETGs in the field at the same redshift (within  $2\sigma$ ), when the mass-size relation is taken into account (see also Cooper et al. 2012; Raichoor et al. 2012; Newman et al. 2013). For clusters in the same redshift range that our structures, the filled square and diamonds are the ETG masses and circularized effective radii from CL J1449+085 at  $z \sim 2$  (Strazzullo et al. 2013) and JKCS 041 at  $z = 1.8$  (Newman et al. 2013), respectively, with masses corrected to a Chabrier IMF. All sizes are measured in the B-band rest-frame. Our structures' ETGs have all masses  $M < 10^{11} M_\odot$ , close to the masses of passive ETGs in CL J1449+085, and about an order

of magnitude lower than the most massive ETGs in JKCS 041.

As a reference, we show the SDSS mass-size relation for ETG and LTG galaxies from Bernardi et al. (2012). While Bernardi et al. mass-size relation has been estimated for field galaxies, it also holds for galaxy cluster for the ETGs (Huertas-Company et al. 2013b), and we don't expect large variations for the LTGs (Fernandez-Lorenzo et al. 2013). Our structures' LTGs lie on the same mass-size relation as Bernardi et al. (2012) LTGs. For the ETGs, assuming that the form of the mass-size relation from Bernardi et al. (2012) does not evolve with redshift, when extrapolating the Delaye et al. (2013) and Lani et al. (2013) mass-size relations at lower masses, our structures' ETGs follow the same mass-size relation at  $1 < z < 2$ .

It is very interesting, because this is also true for the ETGs in JKCS 041 and CL J1449+085. To better quantify this point, in Fig. 7, we plot the mass-normalized B-band rest-frame size,  $\gamma$ , as a function of redshift, for passive ETGs in clusters at  $0.7 < z < 1.6$  from Delaye et al. (2014), JKCS 041 at  $z = 1.8$  (from Newman et al. 2013) and CL J1449+085 at  $z \sim 2$  (from Strazzullo et al. 2013), and the star-forming ETGs in HUDFJ0332.4-2746.6 from this work. Since our galaxies span a large range in mass ( $10^{9.5} M_\odot \lesssim M \lesssim 10^{12} M_\odot$ ), we calculate  $\gamma$  using the SDSS mass-size relation in Bernardi et al. (2012; Eq. 1), instead of the commonly used power law that holds for galaxy masses  $M > 10^{11} M_\odot$ :

$$\log(\gamma) = \log(R_e) + c1 \times \left[ \log\left(\frac{M}{10^{11} M_\odot}\right) \right] + c2 \times \left\{ [\log(M)]^2 - [\log(10^{11} M_\odot)]^2 \right\}$$

where  $R_e$  and  $M$  are the galaxy circularized effective radius and mass in units of  $M_\odot$ , respectively, and  $10^{11} M_\odot$  is the typical mass used for the mass normalization.  $c1$  and  $c2$  are the coefficients for ETGs and LTGs from Bernardi et al. (2012). The uncertainties have all been estimated by bootstrap with replacement, with 1,000 iterations. Both the quiescent and the star-forming ETG median normalized sizes do not evolve significantly from  $z \sim 2$  to  $z \sim 0.7$  ( $\sim 20\%$ ). When using the average  $\gamma$  instead of the median, results are consistent. This redshift range corresponds to a time interval of

$\sim 4$  Gyrs, over which ETG sizes must have evolved on average according to the same mass—size relation as that of cluster ETGs at  $z \sim 1$ .

On the low mass end side ( $M < 10^{11} M_{\odot}$ ), our structures’s ETGs must have had their star formation quenched, though, to be selected as passive ETGs in the  $z \approx 1$  samples.

## 6. Discussion and conclusions

Deep mid-infrared surveys, and space and ground-based infrared spectroscopy have enabled the discovery of clusters of galaxies at redshift  $z = 1.5 - 2$ , an epoch largely unexplored until recently. Most of these discoveries have been based on the searches for star-forming galaxy overdensities around radio sources, and/or red galaxy overdensities in the mid-infrared with Spitzer IRAC. The advent of the HST WFC3 grism and ground-based infrared spectroscopy permit confirmation of these discoveries as real galaxy overdensities (Stanford et al. 2012; Zeinman et al. 2012; Gobat et al. 2013; Newman et al. 2013).

Current X-ray and SZ observations probe cluster virialization through the detection of the hot gas in the gravitational potential well, down to cluster masses of  $\approx 10^{14} M_{\odot}$  and up to redshift  $z \approx 1$ . At higher redshifts, only the extreme end of the cluster mass function can be detected by current instruments. A few objects at  $1.5 < z < 2$  correspond to significant X-ray detections and were identified as already virialized (Andreon et al. 2010; Gobat et al. 2011; Santos et al. 2011; Stanford et al. 2012; Mantz et al. 2014). Two of them also show a significant SZ signal (Brodwin et al. 2012; Mantz et al. 2014). Their cluster masses cover the range  $M_{200} \approx (0.5-4) \times 10^{14} M_{\odot}$ . The other detections (e.g., less massive objects) can only currently be identified as significant red galaxy overdensities, without confirmation of virialization by the detection of hot gas. Depending on the presence or not of the red sequence and their richness, these objects have been identified as clusters or proto-clusters (e.g., Pentericci et al. 2000; Miley et al. 2004, 2006; Venemans 2007; Kuiper et al. 2010; Hatch et al. 2011).

In this paper, we presented the discovery of two star-forming galaxy overdensities in the HUDF using HST WFC3 grism spectroscopy and imaging observations from the CANDELS and 3D-

HST Treasury programs. The richest overdensity, HUDFJ0332.4-2746.6, includes 18 spectroscopic members, of which 6 are ETGs. The other one, HUDFJ0332.5-2747.3, includes 7 spectroscopic members, of which 3 are ETGs. Our detections are mostly based on line emitter galaxy overdensities, similarly to current proto-cluster discoveries at  $z > 2$ , and differently from current cluster detections at the same redshift that are based on red galaxy overdensities. We confirmed the grism redshifts using deep far-UV photometry from the UVUDF (Teplitz et al. 2013).

Using a Nth-nearest neighbor distance estimator and the density contrast, we measure a galaxy overdensity at  $\sim 20\sigma$  and  $\sim (4-7)\sigma$  above the background, for HUDFJ0332.4-2746.6 and HUDFJ0332.5-2747.3, respectively. From HUDFJ0332.4-2746.6 velocity dispersion, we obtain a mass estimate of  $M_{200} = (2.2 \pm 1.8) \times 10^{14} M_{\odot}$ , consistent with the lack of extended X-ray emission. In Table 2, we compare our newly discovered structure to already known clusters, proto-clusters and groups at  $z = 1.6 - 2$ . Within the uncertainties, HUDFJ0332.4-2746.6 has the properties characteristic of a proto-cluster, because of its overdensity and estimated mass, and HUDFJ0332.5-2747.3 those of a galaxy group, because of its overdensity.

Predictions from numerical simulation predictions (Cohn et al. 2005; Li et al. 2007; Chiang et al. 2013) suggest that HUDFJ0332.4-2746.6 is most probably a progenitor of  $M_{200} \approx 10^{14} M_{\odot}$  galaxy clusters at  $z \sim 1$  and of  $M_{200} \approx \text{few} \times 10^{14} M_{\odot}$  galaxy clusters at the present. At  $z \approx 1.8 - 1.9$  Chiang et al. (2013) predict the comoving effective sizes of clusters of mass  $M_{200} \approx 10^{14} M_{\odot}$  to be  $\approx 2 - 5$  Mpc. Their total mass extends beyond this spatial scale, based on the cosmological N-body simulation from the Millennium Run (Springel et al. 2005) and semi-analytic galaxy catalogs from Guo et al. (2011). According to these predictions (see also Shattow et al. 2013), in the comoving  $\sim 1$  Mpc area of the HUDF, we are observing only part of the galaxies that will make up the final galaxy clusters, with other proto-cluster members probably extending over an area approximately ten times larger. Within the GOODS-CDFS area covered by the Guo et al. (2013) photometric redshift catalog, we searched for such overdensities in photo-

metric redshift ranges around the two overdensities. With respect to completeness and purity, the optimal photometric redshift range covering both overdensities is  $1.76 < z_{phot} < 2.1$ . In fact, given the precision on photometric redshift, we cannot separate the two structures (see also Gobat et al. 2013). In this range, we find that 20 of the 35 galaxies that have good (flag 1 to 3) grism spectroscopy have  $1.81 < z_{grism} < 1.93$  (57% purity), and 70% of the galaxies with good grism spectroscopy in the range  $1.81 < z_{grism} < 1.93$  have photometric redshifts  $1.76 < z_{phot} < 2.1$  (70% completeness). In this photometric redshift range, we did not find any other significant overdensity in the area.

We estimate that at most  $\approx 40\%$  of the proto-cluster members are ETGs, against the 80% observed in clusters of galaxies at  $z \approx 1 - 1.5$  (e.g., Postman et al. 2005; Mei et al. 2009; Mei et al. 2012). About 50% of the structure members show possible interactions or disturbed morphologies (asymmetries, faint substructures, tails), which are possible signatures of merger remnants.

Our results are similar to the fractions of ETGs with mass  $M > 10^{10} M_{\odot}$  obtained from Mortlock et al. (2014) in the CANDELS Ultra-Deep Survey (UDS). This suggests the existence of significant overdensities that have similar ETG fractions as the field. It is also interesting that Mortlock et al. found that  $z \sim 1.85$  is a redshift of transition between an epoch in which irregular galaxy fractions dominate over disk galaxy fractions to an epoch in which the trend is inverted to the type fractions observed in the local Universe. For galaxy clusters and proto-clusters at  $z = 1.6 - 1.9$ , the ETG fractions can be quite different in different objects, going from 50% (Gobat 2012; Zeinman et al. 2012; Muzzin et al. 2013) to 80% (Papovich et al. 2012). The two newly discovered overdensities in this paper show the lowest ETG fractions detected so far.

Using multi-wavelength photometry from Guo et al. (2013), we study the two structures' galaxy colors, and find that their red sequence is not yet in place. All the confirmed ETG members, but two, show emission lines that indicate recent star formation activity. Only one ETG show colors consistent with those characteristic of an old stellar population at these redshifts, e.g., all the others have active stellar populations. This is consis-

tent with the fact that most of the ETGs in the two structures are star-forming and will be quenched only at a later time.

From both the two structures' ETG fractions and their colors, new ETGs would need to be formed (e.g., by transformations of LTGs by environmental effects; e.g., Boselli & Gavazzi 2006) or accreted, to obtain the higher ETG fractions observed at lower redshifts. The progenitors of some of these newly transformed ETGs could have been observed as a passive bulge-dominated LTG population in clusters and dense regions at  $z = 1 - 1.3$  (Bundy et al. 2010; Mei et al. 2006ab, 2012; George et al. 2013).

Current red sequence galaxies are predicted to form the bulk of their stars at an average formation redshift  $z_f = 2 - 3$  from both the interpretation of their scaling relations and age and metallicity measurements (e.g., Thomas et al. 2005), and semianalytic models based on the Millennium simulation (e.g., De Lucia & Blaizot 2007; Barro et al. 2013b; Shankar et al. 2013). This implies that their progenitors at  $z \approx 2$  are star-forming galaxies. Combined deep high resolution space imaging and grism spectroscopy permitted us to spectroscopically confirm star-forming blue ETG progenitors. At least part of the red sequence ETGs are already ETGs and compact before quenching their star formation. Our results are consistent with recent observations in the HUDF and modeling by Barro et al. (2013a,b) that demonstrated how compact star-forming galaxies (all morphology selected) show to be progressively quenched from  $z = 2 - 3$  to  $z = 1 - 2$ . In this work, we spectroscopically confirm for the first time the presence of star-forming blue compact ETGs in proto-clusters. Since star-forming ETGs are rare both in clusters and the field up to  $z \approx 1.5$  (e.g., Mei et al. 2009; Huertas-Company et al. 2010; Brodwin et al. 2013; Barro et al. 2013ab, and references therein), the star-forming ETGs are most probably (at least part of) the progenitors of passive ETGs in galaxy clusters at  $z \sim 1 - 1.5$ .

We compare the masses and the sizes of the structures' star-forming blue ETGs with those of passive ETGs in dense regions and galaxy clusters at  $z = 1 - 2$ , and find that they lie on the same mass-size relation. Interestingly, quiescent ETGs in galaxy clusters at  $z = 1.8 - 2$  show a similar behavior as our structure's blue star-

forming ETGs, and the mass-normalized B-band rest-frame size,  $\gamma$ , does not significantly evolve in the redshift range  $0.7 < z < 2$ , contrary to field ETGs (Damjanov et al. 2011; Cimatti et al. 2012; Newman et al. 2013). This implies that, if these objects are the progenitors of quiescent ETGs in clusters at  $z = 1 - 1.5$ , their mass-size relation did not evolve significantly even if their star-formation was quenched; galaxies could increase their mass, simultaneously increasing their size according to this relation.

The diversity of these structures shows how overdensities at  $z > 1.5$  have less homogeneous galaxy populations than those at  $z < 1.5$ . Large studies of clusters and proto-clusters at these higher redshift have to quantify how detection techniques impact their sample selection function, to obtain good statistics of their galaxy population.

## 7. Summary

We found star-forming blue ETGs in two newly discovered galaxy overdensities at  $z = 1.84$  and  $z = 1.9$  in the HUDF. We summarize here our main results:

- We discovered two galaxy overdensities in the HUDF. The first is identified as a galaxy proto-cluster at  $z = 1.84 \pm 0.01$ , HUDFJ0332.4-2746.6, and includes 18 spectroscopic members, for a galaxy overdensity of  $\sim 20\sigma$ . The second is a galaxy group at  $z = 1.90 \pm 0.01$ , HUDFJ0332.5-2747.3, with 7 spectroscopic members, and a galaxy overdensity of  $\sim 4 - 7\sigma$ . From its velocity dispersion, we obtain a mass estimate for HUDFJ0332.4-2746.6 of  $M_{200} = (2.2 \pm 1.8) \times 10^{14} M_{\odot}$ , consistent with the lack of extended X-ray emission.
- The two structures have not yet formed a red sequence. For the first time, we confirm a significant presence of star-forming blue ETGs in dense environments at  $z \sim 1.8 - 1.9$ . We classified 7 and 3 ETGs in HUDFJ0332.4-2746.6 and HUDFJ0332.5-2747.3, respectively, of which 5 have  $J_{125} < 24.5$  mag. The ETG fraction in both structures is at most  $\sim 40\%$ , similar to fractions obtained in the field at these redshifts (Mort-

lock et al. 2014) and less than what is observed in galaxy clusters at the same redshifts ( $\sim 50 - 80\%$ ; Gobat 2012; Papovich et al. 2012; Zeinman et al. 2012; Muzzin et al. 2013) and at  $z < 1.5$  ( $80\%$ ; e.g., Postman et al. 2005; Desai et al. 2007; Mei et al. 2009; Mei et al. 2012). This suggests that large overdensities at  $z > 1.5$  have more diverse galaxy populations than those at  $z < 1.5$ , and that it is essential to quantify how detection techniques impact our cluster/proto-cluster selection function.

- About 50% of the structure members show possible interactions or disturbed morphologies, with asymmetries, faint substructures, and tails, all possible signatures of merger remnants.
- The star-forming blue ETG have masses  $8.9 \lesssim \log_{10}(\frac{M}{M_{\odot}}) \lesssim 10.8$ , and their mass-size relation lies on the same mass-size relation observed for quiescent ETGs in clusters and dense regions at  $z = 0.7 - 2$  (Lani et al. 2013; Newman et al. 2013; Strazzullo et al. 2013; Delaye et al. 2014). Interestingly, quiescent ETG sizes in clusters also do not evolve significantly in this redshift range, which covers  $\sim 4$  Gyr in time. This suggest that at these epochs, cluster ETGs do not significantly change their median/average sizes, and evolve according to a mass-size relation similar to the one at  $z \sim 1$ .
- Both the two structures' ETG fractions and their colors suggest that these star-forming blue ETGs are the most likely progenitors of at least part of the passive ETGs observed in clusters at  $z < 1$ . Their masses are  $\sim 3 - 5$  times lower than the most massive ETGs in these lower redshift clusters. More (massive) ETGs have to be formed/accreted and then quenched, to obtain the ETG fractions, colors, and masses observed in clusters at  $z < 1$ .

Small samples can be hardly representative of the larger populations, but as with other studies at these high redshifts, we discover new objects often one by one, and we are consistently building larger samples that will improve our understanding of cluster formation and evolution. The CANDELS and 3D-HST Treasury programs have

opened a new path for proto-cluster detection in this redshift range.

Surveys of this kind point to the capabilities of future space missions, such as Euclid (Laureijs et al. 2011) and WFIRST (Thompson et al. 2013). Those missions have the potential to discover a large population of young clusters at all redshifts, and especially at these very early epochs of cluster formation and assembly.

This work is based in part on observations made with the Spitzer Space Telescope, which is operated by the Jet Propulsion Laboratory, California Institute of Technology under a contract with NASA.

*Facilities:* HST(ACS and WFC3), Spitzer (IRAC)

## REFERENCES

- Andreon, S., Maughan, B., Trinchieri, G., & Kurk, J. 2009, *A&A*, 507, 147
- Andreon, S., & Huertas-Company, M. 2011, *A&A*, 526, A11
- Andreon, S., Newman, A. B., Trinchieri, G., et al. 2013, arXiv:1311.4361
- Arnouts, S., et al. 2002, *MNRAS*, 329, 355
- Ashby, M. L. N., Stanford, S. A., Brodwin, M., et al. 2013a, *ApJS*, 209, 22
- Ashby, M. L. N., Willner, S. P., Fazio, G. G., et al. 2013b, *ApJ*, 769, 80
- Barro, G., Faber, S. M., Pérez-González, P. G., et al. 2013a, *ApJ*, 765, 104
- Barro, G., Faber, S. M., Perez-Gonzalez, P. G., et al. 2013b, arXiv:1311.5559
- Bassett, R., Papovich, C., Lotz, J. M., et al. 2013, *ApJ*, 770, 58
- Beckwith, S. V. W., Stiavelli, M., Koekemoer, A. M., et al. 2006, *AJ*, 132, 1729
- Bernardi, M., Meert, A., Vikram, V., et al. 2012, arXiv:1211.6122
- Bertin, E. & Arnouts, S. 1996, *A&AS*, 117, 393
- Bird, C. M., & Beers, T. C. 1993, *AJ*, 105, 1596
- Boselli, A., & Gavazzi, G. 2006, *PASP*, 118, 517
- Brammer, G. B., van Dokkum, P. G., Franx, M., et al. 2012, *ApJS*, 200, 13
- Brodwin, M., Gonzalez, A. H., Stanford, S. A., et al. 2012, *ApJ*, 753, 162
- Brodwin, M., Stanford, S. A., Gonzalez, A. H., et al. 2013, arXiv:1310.6039
- Bruzual A., G. & Charlot, S. 2003, *MNRAS*, 344, 1000 (BC03)
- Bundy, K., Scarlata, C., Carollo, C. M., et al. 2010, *ApJ*, 719, 1969
- Calzetti, D., Armus, L., Bohlin, R. C., Kinney, A. L., Koornneef, J., & Storchi-Bergmann, T. 2000, *ApJ*, 533, 682
- Carlberg, R. G. et al. 1997, *ApJL*, 485, L13
- Castellano, M., Salimbeni, S., Trevese, D., et al. 2007, *ApJ*, 671, 1497
- Castellano, M., Pentericci, L., Menci, N., et al. 2011, *A&A*, 530, A27
- Chabrier, G. 2003, *PASP*, 115, 763
- Chiaberge, M., Capetti, A., Macchetto, F. D., et al. 2010, *ApJ*, 710, L107
- Chiang, Y.-K., Overzier, R., & Gebhardt, K. 2013, *ApJ*, 779, 127
- Cimatti, A., Nipoti, C., & Cassata, P. 2012, *MNRAS*, 422, L62
- Colbert, J. W., Teplitz, H., Atek, H., et al. 2013, *ApJ*, 779, 34
- Cohn, J. D., & White, M. 2005, *Astroparticle Physics*, 24, 316
- Conselice, C. J. 2003, *ApJS*, 147, 1
- Cooper, M. C., Newman, J. A., Weiner, B. J., et al. 2008, *MNRAS*, 383, 1058
- Cooper, M. C., Griffith, R. L., Newman, J. A., et al. 2012, *MNRAS*, 419, 3018
- Damjanov, I., Abraham, R. G., Glazebrook, K., et al. 2011, *ApJ*, 739, L44

- Danese, L., de Zotti, G., & di Tullio, G. 1980, *A&A*, 82, 322
- De Lucia, G., & Blaizot, J. 2007, *MNRAS*, 375, 2
- Delaye, L., Huertas-Company, M., Mei, S., et al. 2014, arXiv:1307.0003
- Desai, V., et al. 2007, *ApJ*, 660, 1151
- Dressler, A. 1980, *ApJ*, 236, 351
- Eisenhardt, P. R. M., Brodwin, M., Gonzalez, A. H., et al. 2008, *ApJ*, 684, 905
- Elbaz, D., Daddi, E., Le Borgne, D., et al. 2007, *A&A*, 468, 33
- Ellis, R. S., McLure, R. J., Dunlop, J. S., et al. 2013, *ApJ*, 763, L7
- Evrard, A. E., Bialek, J., Busha, M., et al. 2008, *ApJ*, 672, 122
- Fassbender, R., Nastasi, A., Böhringer, H., et al. 2011, *A&A*, 527, L10
- Fazio, G. G., Hora, J. L., Allen, L. E., et al. 2004, *ApJS*, 154, 10
- Fernández Lorenzo, M., Sulentic, J., Verdes-Montenegro, L., & Argudo-Fernández, M. 2013, *MNRAS*, 434, 325
- Galametz, A., Stern, D., De Breuck, C., et al. 2012, *ApJ*, 749, 169
- George, M. R., Ma, C.-P., Bundy, K., et al. 2013, *ApJ*, 770, 113
- Gladders, M. D., & Yee, H. K. C. 2000, *AJ*, 120, 2148
- Gobat, R., Daddi, E., Onodera, M., et al. 2011, *A&A*, 526, A133
- Gobat, R., Strazzullo, V., Daddi, E., et al. 2013, arXiv:1305.3576
- Grogin, N. A., Kocevski, D. D., Faber, S. M., et al. 2011, *ApJS*, 197, 35
- Grützbauch, R., Conselice, C. J., Bauer, A. E., et al. 2011, *MNRAS*, 418, 938
- Guo et al., 2013, *ApJS*, in press
- Hatch, N. A., Kurk, J. D., Pentericci, L., et al. 2011, *MNRAS*, 415, 2993
- Hayashi, M., Kodama, T., Koyama, Y., Tadaki, K.-I., & Tanaka, I. 2011, *MNRAS*, 415, 2670
- Hatch, N. A., De Breuck, C., Galametz, A., et al. 2011, *MNRAS*, 410, 1537
- Huertas-Company, M., Tasca, L., Rouan, D., et al. 2009, *A&A*, 497, 743
- Huertas-Company, M., Aguerri, J. A. L., Tresse, L., et al. 2010, *A&A*, 515, A3
- Huertas-Company, M., Aguerri, J. A. L., Bernardi, M., Mei, S., & Sánchez Almeida, J. 2011, *A&A*, 525, A157
- Huertas-Company, M., Mei, S., Shankar, F., et al. 2013a, *MNRAS*, 428, 1715
- Huertas-Company, M., Shankar, F., Mei, S., et al. 2013b, *ApJ*, 779, 29
- Ichikawa, T., Suzuki, R., Tokoku, C., et al. 2006, *Proc. SPIE*, 6269,
- Ilbert, O., et al. 2006, *A&A*, 457, 841
- Ilbert, O., et al. 2010, *ApJ*, 709, 644
- Illingworth, G. D., Magee, D., Oesch, P. A., et al. 2013, arXiv:1305.1931
- Kartaltepe, J. S., Mozena, M., Kocevski, D., et al. 2014, arXiv:1401.2455
- Kodama, T., Tanaka, I., Kajisawa, M., et al. 2007, *MNRAS*, 377, 1717
- Koekemoer, A. M., Faber, S. M., Ferguson, H. C., et al. 2011, *ApJS*, 197, 36
- Koekemoer, A. M., Ellis, R. S., McLure, R. J., et al. 2013, *ApJS*, 209, 3
- Koyama, Y., Smail, I., Kurk, J., et al. 2013, *MNRAS*, 1677
- Kuiper, E., Hatch, N. A., Röttgering, H. J. A., et al. 2010, *MNRAS*, 405, 969
- Kümmel, M., Walsh, J. R., Pirzkal, N., Kuntschner, H., & Pasquali, A. 2009, *PASP*, 121, 59

- Kuntschner, H., Bushouse, H., Kümmel, M., Walsh, J. R., & MacKenty, J. 2010, *Proc. SPIE*, 7731,
- Kurk, J., Cimatti, A., Zamorani, G., et al. 2009, *A&A*, 504, 331
- Kurk, J., Cimatti, A., Daddi, E., et al. 2013, *A&A*, 549, A63
- Laidler, V. G., Papovich, C., Grogan, N. A., et al. 2007, *PASP*, 119, 1325
- Lani, C., Almaini, O., Hartley, W. G., et al. 2013, *MNRAS*, 435, 207
- Laureijs, R., Amiaux, J., Arduini, S., et al. 2011, *arXiv:1110.3193*
- Li, Y., Mo, H. J., van den Bosch, F. C., & Lin, W. P. 2007, *MNRAS*, 379, 689
- Liu, F. S., Guo, Y., Koo, D. C., et al. 2013, *ApJ*, 769, 147
- Lotz, J. M., Papovich, C., Faber, S. M., et al. 2013, *ApJ*, 773, 154
- MacKenty, J. W. & Smith, L. 2012, CTE White Paper, Tech. rep., STScI
- Mantz, A. B., Abdulla, Z., Carlstrom, J. E., et al. 2014, *arXiv:1401.2087*
- McLean, I. S., Steidel, C. C., Epps, H., et al. 2010, *Proc. SPIE*, 7735,
- McLean, I. S., Steidel, C. C., Epps, H. W., et al. 2012, *Proc. SPIE*, 8446,
- Mei, S., Blakeslee, J. P., Stanford, S. A., et al. 2006a, *ApJ*, 639, 81
- Mei, S., Holden, B. P., Blakeslee, J. P., et al. 2006b, *ApJ*, 644, 759
- Mei, S., Holden, B. P., Blakeslee, J. P., et al. 2009, *ApJ*, 690, 42
- Mei, S., Stanford, S. A., Holden, B. P., et al. 2012, *ApJ*, 754, 141
- Miley, G. K., Overzier, R. A., Tsvetanov, Z. I., et al. 2004, *Nature*, 427, 47
- Miley, G. K., Overzier, R. A., Zirm, A. W., et al. 2006, *ApJ*, 650, L29
- Mortlock, A., Conselice, C. J., Hartley, W. G., et al. 2013, *MNRAS*, 433, 1185
- Munari, E., Biviano, A., Borgani, S., Murante, G., & Fabjan, D. 2013, *MNRAS*, 430, 2638
- Muzzin, A., Wilson, G., Demarco, R., et al. 2013, *ApJ*, 767, 39
- Navarro, J. F., Frenk, C. S., & White, S. D. M. 1996, *ApJ*, 462, 563
- Newman, A. B., Ellis, R. S., Bundy, K., & Treu, T. 2012, *ApJ*, 746, 162
- Newman, A. B., Ellis, R. S., Andreon, S., et al. 2013, *arXiv:1310.6754*
- Oke, J. B., & Gunn, J. E. 1983, *ApJ*, 266, 713
- Papovich, C., Momcheva, I., Willmer, C. N. A., et al. 2010, *ApJ*, 716, 1503
- Papovich, C., Bassett, R., Lotz, J. M., et al. 2012, *ApJ*, 750, 93
- Peng, C. Y., Ho, L. C., Impey, C. D., & Rix, H. 2002, *AJ*, 124, 266
- Peng, C. Y., Ho, L. C., Impey, C. D., & Rix, H.-W. 2010, *AJ*, 139, 2097
- Pentericci, L., Kurk, J. D., Röttgering, H. J. A., et al. 2000, *A&A*, 361, L25
- Poggianti, B. M., Calvi, R., Bindoni, D., et al. 2013, *ApJ*, 762, 77
- Popesso, P., Biviano, A., Rodighiero, G., et al. 2012, *A&A*, 537, A58
- Postman, M. et al., 2005, *ApJ*, 623, 721
- Raichoor, A., Mei, S., Stanford, S. A., et al. 2012, *ApJ*, 745, 130
- Rettura, A., Rosati, P., Nonino, M., et al. 2010, *ApJ*, 709, 512
- Rigby, E. E., Hatch, N. A., Röttgering, H. J. A., et al. 2013, *MNRAS*, 2671
- Rykoff, E. S., Evrard, A. E., McKay, T. A., et al. 2008, *MNRAS*, 387, L28
- Salimbeni, S., Castellano, M., Pentericci, L., et al. 2009, *A&A*, 501, 865

- Santos, J. S., Fassbender, R., Nastasi, A., et al. 2011, *A&A*, 531, L15
- Santos, J. S., Altieri, B., Tanaka, M., et al. 2014, *MNRAS*, 438, 2565
- Scoville, N., Arnouts, S., Aussel, H., et al. 2013, *ApJS*, 206, 3
- Shankar, F., Marulli, F., Bernardi, M., et al. 2013, *MNRAS*, 428, 109
- Shankar, F., Mei, S., Huertas-Company, M., et al. 2014, *MNRAS*, 344
- Sharples, R., Bender, R., Bennett, R., et al. 2006, *New A Rev.*, 50, 370
- Shattow, G. M., Croton, D. J., Skibba, R. A., et al. 2013, *MNRAS*, 433, 3314
- Sirianni, M. et al. 2005, *PASP*, 117, 1049
- Snyder, G. F., Brodwin, M., Mancone, C. M., et al. 2012, *ApJ*, 756, 114
- Stanford, S. A., Brodwin, M., Gonzalez, A. H., et al. 2012, *ApJ*, 753, 164
- Steidel, C. C., Adelberger, K. L., Dickinson, M., et al. 1998, *ApJ*, 492, 428
- Strazzullo, V., Gobat, R., Daddi, E., et al. 2013, *ApJ*, 772, 118
- Tadaki, K., Kodama, T., Ota, K., et al. 2012, *MNRAS*, 423, 2617
- Tanaka, M., Finoguenov, A., & Ueda, Y. 2010, *ApJ*, 716, L152
- Tanaka, M., Finoguenov, A., Mirkazemi, M., et al. 2013, *PASJ*, 65, 17
- Teplitz, H. I., Rafelski, M., Kurczynski, P., et al. 2013, *AJ*, 146, 159
- Thomas, D., Maraston, C., Bender, R., & Mendes de Oliveira, C. 2005, *ApJ*, 621, 673
- Thompson, R., Green, J., Rieke, G., et al. 2013, *arXiv:1312.4548*
- Tran, K.-V. H., Papovich, C., Saintonge, A., et al. 2010, *ApJ*, 719, L126
- van Dokkum, P., Brammer, G., Momcheva, I., et al. 2013, *arXiv:1305.2140*
- van der Wel, A., Bell, E. F., Häussler, B., et al. 2012, *ApJS*, 203, 24
- Vulcani, B., Poggianti, B. M., Oemler, A., et al. 2013, *A&A*, 550, A58
- White, M., Cohn, J. D., & Smit, R. 2010, *MNRAS*, 408, 1818
- Wylezalek, D., Galametz, A., Stern, D., et al. 2013, *ApJ*, 769, 79
- Xue, Y. Q., Luo, B., Brandt, W. N., et al. 2011, *ApJS*, 195, 10
- Zeimann, G. R., Stanford, S. A., Brodwin, M., et al. 2012, *ApJ*, 756, 115
- Ziparo, F., Popesso, P., Finoguenov, A., et al. 2013, *MNRAS*, 2575



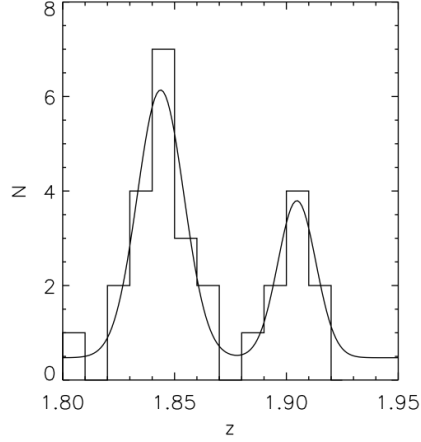


Fig. 1.— The redshift distribution of HUDFJ0332.4-2746.6 and HUDFJ0332.5-2747.3 spectroscopic members. The continuous line is the double Gaussian fit described in the text.

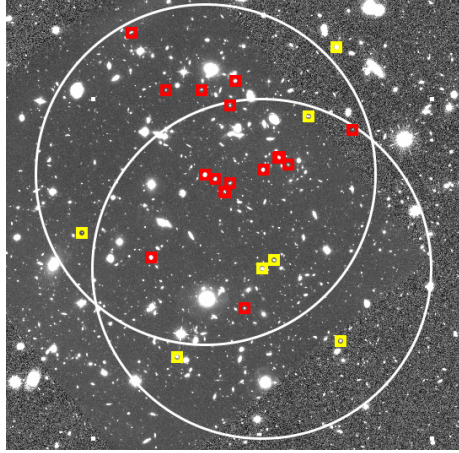


Fig. 2.— Our structures' galaxies. Over the  $H_{160}$  image of the HUDF, the red and yellow boxes show spectroscopic members, for HUDFJ0332.4-2746.6 and HUDFJ0332.5-2747.3, respectively. Both UDF-2090 and UDF-2103, and UDF-2433 and UDF-2491, are pairs and cannot be distinguished in the figure. The large white circles, centered on each structure, have radius  $R = 1'$ , that corresponds to a comoving radius of  $\approx 0.5$  Mpc. Most of HUDFJ0332.4-2746.6 are within  $1'$  from the structure center, the only exception is GMASS220. HUDFJ0332.5-2747.3 is more sparse. North is on the top, East on the left.



Fig. 3.— HUDFJ0332.4-2746.6 : Combined color image of the spectroscopic members, from the ACS  $B_{435}$ , WFC3  $i_{775}$  and  $H_{160}$  images. Most of galaxies present spiral morphologies, as expected from most star-forming galaxies. Seven are classified as ETGs. Most show asymmetries, faint substructures and tails, which are signatures of merger remnants. Four galaxies form two confirmed pairs, others have close small companions that are not confirmed to be at the same redshift.



Fig. 4.— HUDFJ0332.5-2747.3 : Combined color image of the spectroscopic members, from the ACS  $B_{435}$ , WFC3  $i_{775}$  and  $H_{160}$  images. Most of galaxies present spiral morphologies, three have early-type morphologies.

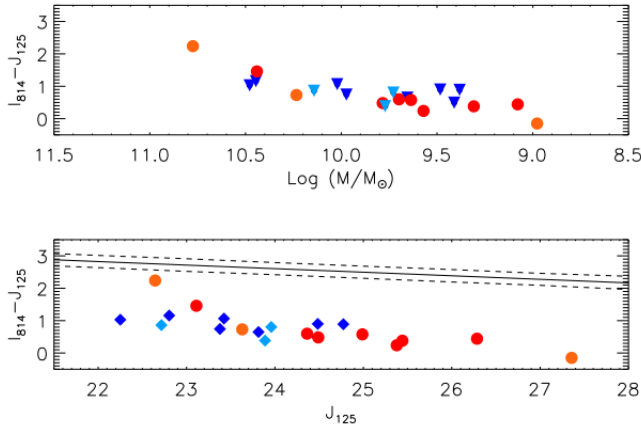


Fig. 5.— Color-magnitude and color-mass diagram for all HUDFJ0332.4-2746.6 and HUDFJ0332.5-2747.3 spectroscopically confirmed members with Guo et al. (2013) photometry. The selected galaxies have masses in the range  $8.9 < \log_{10}(\frac{M}{M_{\odot}}) < 11$ . The  $(I_{814} - J_{125})$  color is close to the  $(U - B)$  rest-frame, and  $J_{125}$  to the B-band rest-frame. Red/orange circles and blue/sky triangles are ETGs and LTGs in HUDFJ0332.4-2746.6/HUDFJ0332.5-2747.3, respectively. We show as a continuous line the color-magnitude relation at  $z \sim 1$  from Mei et al. (2009) passively evolved at  $z=1.84$ , and the dashed lines show a region within 3 times the observed scatter. A red sequence is not yet formed.

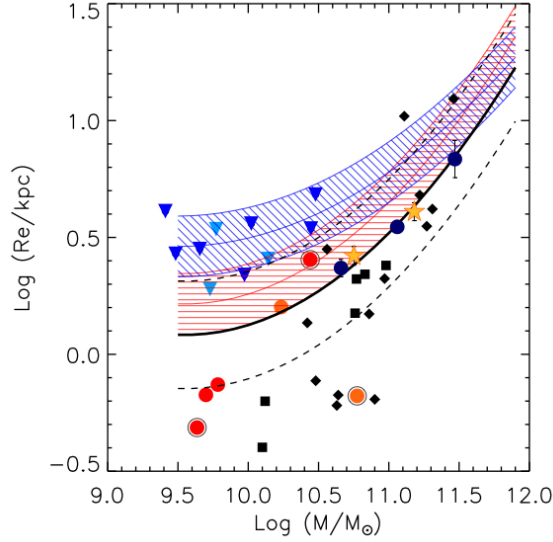


Fig. 6.— The mass-size relation for galaxies with  $H_{160} > 24.5$  mag in HUDFJ0332.4-2746.6 and HUDFJ0332.5-2747.3. Red/orange circles and blue/sky triangles are ETGs and LTGs in HUDFJ0332.4-2746.6/HUDFJ0332.5-2747.3, respectively. The empty circles show galaxies with  $n > 2$ . The two stars show the ETG mass-size relation observed in galaxy clusters at redshift  $1.2 < z < 1.5$  from Delaye et al. (2014), and the dark blue circles show results from Lani et al. (2013) ( $1 < z < 2$ ), for their most dense regions. The filled squares and diamonds are the quiescent ETGs masses and circularized effective radii from CL J1449+085 at  $z = 1.99$  (from Strazzullo et al. 2013) and JKCS 041 at  $z = 1.8$  (from Newman et al. 2013), respectively. All ETGs from CL J1449+085 and JKCS 041 have been selected as galaxies with  $n > 2$ . As a reference, we show the SDSS local mass-size relation from Bernardi et al. (2012). The red/blue continuous line show the mass-size relation for SDSS ETG/LTG, respectively. The shaded regions show the  $1\sigma$  observed scatter. The continuous black line is the local mass-size relation scaled to the average sizes from Delaye et al. at  $10^{11} M_{\odot}$  (the dashed lines indicate the observed scatter). Our blue star-forming ETGs lie on the same mass-size relation as quiescent ETGs in dense environments at  $1 < z < 2$ .

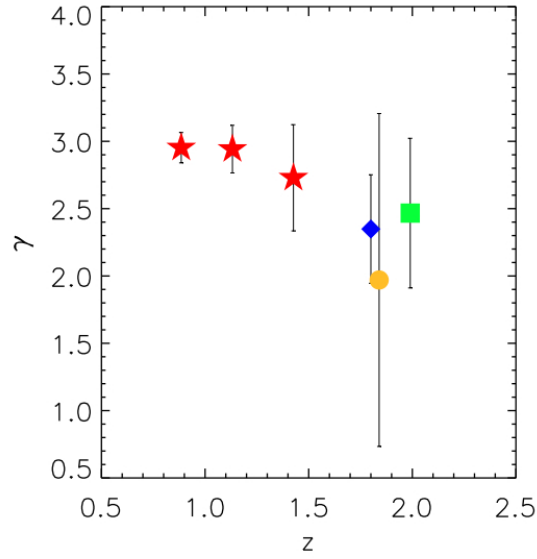


Fig. 7.— The median mass-normalized B-band rest-frame size  $\gamma$ , as a function of redshift. The yellow circle is the median  $\gamma$  for HUDFJ0332.4-2746.6 ETGs. The red stars are the median  $\gamma$ s for quiescent ETGs in clusters at  $0.7 < z < 1.6$  from Delaye et al. (2014). The green square and the blue diamond are the median  $\gamma$ s for quiescent ETGs from CL J1449+085 at  $z = 1.99$  (Strazzullo et al. 2013) and JKCS 041 at  $z = 1.8$  (Newman et al. 2013), respectively. Our structures’ star-forming blue ETGs are consistent with those of quiescent ETGs in dense environments at similar redshifts. Both star-forming and quiescent ETGs in dense environments do not show much evolution in the redshift range  $z = 0.7 - 2$ .

## A. Appendix

In this appendix, we show detections and dropouts from the UVUDF survey (Tepliz et al. 2013). Most of the selected galaxies are *F225W* dropouts, e.g., are not detected in WFC3 *F225W* (the top left panel), but are detected in WFC3 *F336W* (the top right panel). The two exceptions are: UDF 1909 and UDF 1898, that are not detected in *F336W*, but are detected in ACS *F435W*, and are most probably at higher redshift galaxies or have too low surface brightness to be unambiguously identified as  $z = 1.8 - 1.9$  galaxies.

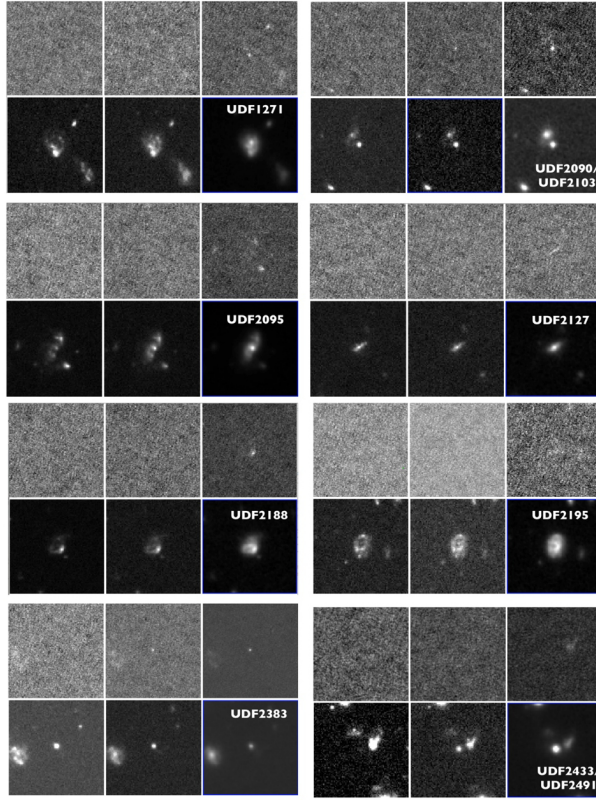


Fig. 8.— HUDFJ0332.4-2746.6 candidates. For each candidate, starting from the top left we show clockwise WFC3  $F_{225W}$ ,  $F_{275W}$  and  $F_{336W}$  from UVUDF, ACS  $F_{435W}$ ,  $I_{814}$  and WFC3  $J_{125}$  images. Galaxies are identified by their 3D-HST ID. The size of each image is  $5''$ . All candidates are  $F_{275W}$  dropouts.

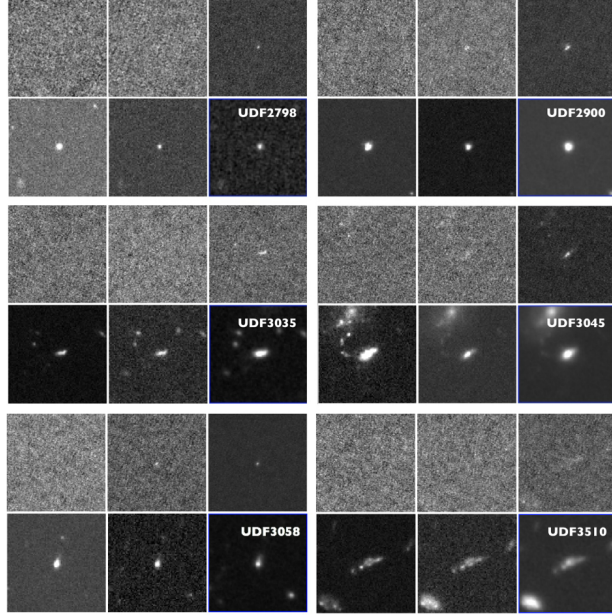


Fig. 9.— HUDFJ0332.4-2746.6 candidates. For each candidate, starting from the top left we show clockwise WFC3  $F_{225W}$ ,  $F_{275W}$  and  $F_{336W}$  from UVUDF, ACS  $F_{435W}$ ,  $I_{814}$  and WFC3  $J_{125}$  images. Galaxies are identified by their 3D-HST ID. The size of each image is  $5''$ . All candidates are  $F_{275W}$  dropouts.

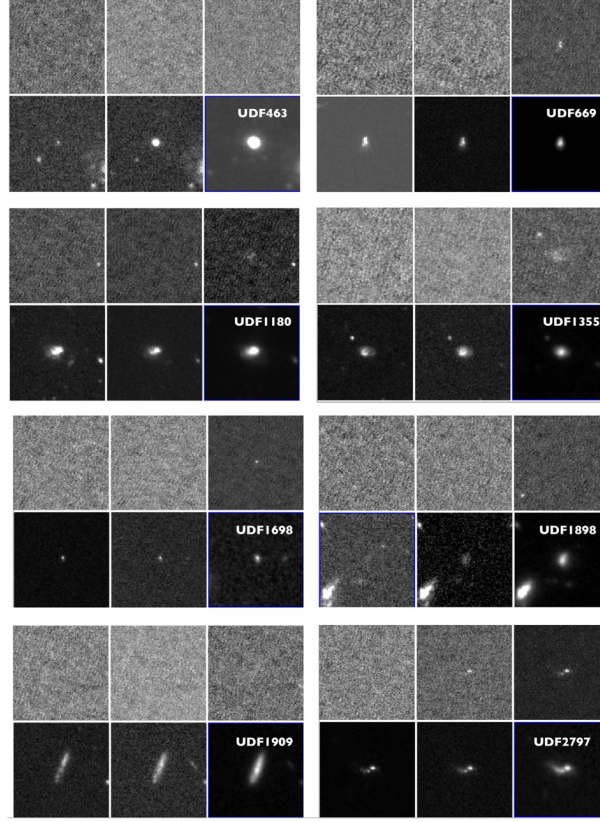


Fig. 10.— HUDFJ0332.5-2747.3 candidates. For each candidate, starting from the top left we show clockwise WFC3  $F_{225W}$ ,  $F_{275W}$  and  $F_{336W}$  from UVUDF, ACS  $F_{435W}$ ,  $I_{814}$  and WFC3  $J_{125}$  images. Galaxies are identified by their 3D-HST ID. The size of each image is  $5''$ . All candidates are  $F_{275W}$  dropouts, but UDF 1909 and UDF 1898. Those two galaxies are not detected in  $F_{336W}$ , but are detected in ACS  $F_{435W}$ , e.g. are  $F_{435W}$  dropouts. They are excluded from our analysis because they are most probably higher redshift galaxies or have too low surface brightness to be unambiguously identified as  $z = 1.8 - 1.9$  galaxies.



Table 1: Spectroscopic members for HUDFJ0332.4-2746.6 and HUDFJ0332.5-2747.3

ID	RA (J2000)	DEC(J2000)	z	Spectral Features (Q)
HUDFJ0332.4-2746.6				
UDF-901	53.15126	-27.79241	$1.841 \pm 0.001$	OIII, H $\beta$ , H $\gamma$
UDF-1271/GMASS-675	53.16166	-27.78743	$1.836 \pm 0.008$	OIII, H $\beta$ (3.3)
UDF-2090	53.15346	-27.78098	$1.849 \pm 0.001$	OIII, H $\gamma$
UDF-2095/GMASS-858	53.15565	-27.77930	$1.839 \pm 0.003$	OIII, H $\beta$ , H $\gamma$ (8.4)
UDF-2103	53.15351	-27.78091	$1.838 \pm 0.004$	OIII
UDF-2127	53.15287	-27.78012	$1.858 \pm 0.003$	OIII
UDF-2188/GMASS-875	53.15452	-27.77972	$1.836 \pm 0.004$	OIII (5.1)
UDF-2195/GMASS-894	53.14921	-27.77880	$1.850 \pm 0.002$	OIII, OIIIx, H $\beta$ , H $\delta$ (4.6)
UDF-2383	53.14642	-27.77831	$1.865 \pm 0.001$	OIII
UDF-2433	53.14744	-27.77761	$1.825 \pm 0.002$	OIII, OIIIx
UDF-2491	53.14744	-27.77761	$1.889 \pm 0.007$	OIII
UDF-2798	53.13924	-27.77485	$1.843 \pm 0.002$	OII, OIII
UDF-2900	53.15288	-27.77250	$1.845 \pm 0.001$	OIII, H $\beta$ , H $\gamma$
UDF-3035 <sup>a</sup>	53.15605	-27.77095	$1.833 \pm 0.004$	OII, OIII, H $\gamma$
UDF-3045	53.15228	-27.77009	$1.848 \pm 0.001$	OIII, H $\beta$ , H $\gamma$
UDF-3058	53.16001	-27.77100	$1.853 \pm 0.002$	OIII
UDF-3510	53.16387	-27.76532	$1.841 \pm 0.003$	OIII, H $\beta$ , H $\gamma$
GMASS220	53.15492	-27.80940	$1.850 \pm 0.001$	Fe, C (4.7)
HUDFJ0332.5-2747.3				
UDF-463	53.15881	-27.79716	$1.904 \pm 0.004$	4000Åbreak
UDF-669	53.14060	-27.79562	$1.909 \pm 0.002$	OIII, H $\beta$ , H $\delta$
UDF-1180	53.14930	-27.78853	$1.907 \pm 0.002$	OIII, OII, H $\beta$ , OIIIx, H $\delta$
UDF-1355	53.14799	-27.78769	$1.884 \pm 0.006$	OIII (4.4)
UDF-1698	53.16935	-27.78499	$1.911 \pm 0.002$	OIII
<i>UDF-1898<sup>a</sup></i>	53.17368	-27.78207	$1.894 \pm 0.058$	<i>OIIIx, H<math>\beta</math></i>
<i>UDF-1909<sup>a</sup></i>	53.14903	-27.78196	$1.917 \pm 0.017$	<i>OIII, H<math>\delta</math></i>
UDF-2797	53.14418	-27.77356	$1.892 \pm 0.001$	OIII, H $\beta$ , H $\delta$ , H $\gamma$
UDF-3297	53.14102	-27.76673	$1.904 \pm 0.006$	4000Åbreak

Galaxies are identified by their 3D-HST ID (UDF; from Brammer et al. 2012) or GMASS ID (GMASS; from Kurk et al. 2013). Redshifts and uncertainties for GMASS are from Kurk et al. (2010; 2013). For the spectral features, OIII and OIIIx indicate the [O III] $\lambda$ 5007 and the [O III] $\lambda$ 4363 emission line, respectively, H $\beta$  the [H $\beta$ ] $\lambda$ 4861 emission line, H $\gamma$  the [H $\gamma$ ] $\lambda$ 4340, and OII the [O II] $\lambda$ 3727. The lines are in italics if they were measured with a  $1 < S/N < 3$ , otherwise they were measured with  $S/N > 3$ . When the galaxies also have a GMASS redshift, in parenthesis is given the GMASS redshift  $S/N$ . The flag (a) means all lines were measured with  $S/N < 1$ . Galaxies with IDs in italic are not considered as structure members because they have low  $S/N$  spectroscopy, and are not detected in the 336W bandpass.

Table 2: Comparison of HUDFJ0332.4-2746.6 and HUDFJ0332.5-2747.3 properties with those of already known clusters, proto-clusters and groups at  $z = 1.6 - 2$

Name	Identification	z	Overdensity	$\sigma_{disp}$ (km/s)	Mass ( $10^{14} \times M_{\odot}$ )	X-ray Lum./Detection ( $10^{43} \text{ erg s}^{-1}$ )	Reference
CL J033211.67-274633.8	Group	1.61	$\sim 5\sigma$	...	$M_{200}^{(a)} = 0.32 \pm 0.08$	$1.8 \pm 0.6$	Tanaka et al.
IRC-0218A/XMM-LSS J02182-05102	Proto-cluster	1.62	$> 20\sigma$	$860 \pm 490$	$M_{200}^{(b)} \sim 0.1 - 0.4$	$> 4\sigma$ Detection	Papovich et al. 2010; 2012
SpARCS J022427-032354	Cluster	1.63	...	...	...	Detection	Muzzin et al. (2013)
IDCS J1426+3508	Cluster	1.75	...	...	$M_{200}^{(a)} \sim 5.6 \pm 1.6$	$55 \pm 12$	Stanford et al. 2012; Brodwin et al. 2012
JKCS 041	Cluster	1.80	...	...	$M_{200}^{(c)} \sim 2$	$76 \pm 5$	Newman et al. 2013; Andreon et al. 2013
HUDFJ0332.4-2746.6	Proto-cluster	1.84	$\sim 20\sigma$	$730 \pm 260$	$M_{200}^{(b)} = 2.2 \pm 1.8$	$< 1 - 6$	This work
IDCS J1433.2+3306	Cluster	1.89	...	...	$M_{200}^{(b)} \sim 1$	...	Zeimann et al. 2012
HUDFJ0332.5-2747.3	Group	1.90	$\sim 4 - 7\sigma$	...	...	...	This work
CL J1449+085	Cluster	1.99	$> 20\sigma$	...	$M_{200}^{(a)} = 0.53 \pm 0.09$	$6.4 \pm 1.8$	Gobat et al. 2013

All estimates are given as they are from the references. For the overdensities,  $\sigma$  is estimated with respect to the background, as given by the references. X-ray fluxes and mass estimates have not been homogenized. (a) and (b) indicate mass estimates derived from the X-ray flux and the velocity dispersion, respectively. (c) indicates that the mass estimate is derived from the X-ray flux and cluster richness.